

# Nanoscale

Accepted Manuscript



This is an *Accepted Manuscript*, which has been through the Royal Society of Chemistry peer review process and has been accepted for publication.

*Accepted Manuscripts* are published online shortly after acceptance, before technical editing, formatting and proof reading. Using this free service, authors can make their results available to the community, in citable form, before we publish the edited article. We will replace this *Accepted Manuscript* with the edited and formatted *Advance Article* as soon as it is available.

You can find more information about *Accepted Manuscripts* in the [Information for Authors](#).

Please note that technical editing may introduce minor changes to the text and/or graphics, which may alter content. The journal's standard [Terms & Conditions](#) and the [Ethical guidelines](#) still apply. In no event shall the Royal Society of Chemistry be held responsible for any errors or omissions in this *Accepted Manuscript* or any consequences arising from the use of any information it contains.

# Retrieving the electronic properties of silicon nanocrystals embedded in a dielectric matrix by low-loss EELS

Alberto Eljarrat,<sup>\*a</sup> Lluís López-Conesa,<sup>a</sup> Julian López-Vidrier,<sup>a</sup> Sergi Hernández,<sup>a</sup> Blas Garrido,<sup>a</sup> César Magén,<sup>b,c</sup> Francesca Peiró,<sup>a</sup> and Sònia Estradé<sup>a, d</sup>

Received Xth XXXXXXXXXX 20XX, Accepted Xth XXXXXXXXXX 20XX

First published on the web Xth XXXXXXXXXX 200X

DOI: 10.1039/b000000x

In this work we apply low-loss electron energy loss spectroscopy (EELS) to probe structural and electronic properties of single silicon nanocrystals (NCs) embedded in three different dielectric matrices (SiO<sub>2</sub>, SiC and Si<sub>3</sub>N<sub>4</sub>). A monochromated and aberration corrected transmission electron microscope has been operated at 80 kV to avoid sample damage and to reduce the impact of radiative losses. We present a novel approach to disentangle the electronic features corresponding to pure Si-NCs from the surrounding dielectric material contribution through an appropriated computational treatment of hyperspectral datasets. First, the different material phases have been identified by measuring the plasmon energy. Due to the overlapping of Si-NCs and dielectric matrix information, the variable shape and position of mixed plasmonic features increases the difficulty for non-linear fitting methods to identify and separate the components in the EELS signal. We have managed to solve this problem for silicon oxide and nitride systems by applying multivariate analysis methods that can factorize the hyperspectral datacubes in selected regions. By doing so, the EELS spectra are re-expressed as a function of abundance of Si-NC-like and dielectric-like factors. EELS contributions from the embedded nanoparticles as well as their dielectric surroundings are thus studied in a new light, and compared with the dielectric material and crystalline silicon from the substrate. Electronic properties such as bandgaps and plasmon shifts can be obtained by straightforward examination. Finally, we have calculated the complex dielectric functions, and the related electron effective mass and density of valence electrons.

## 1 Introduction

Because of the high availability and low cost of the technological processes involved, silicon-based devices represent the dominant technology for photovoltaic applications both at research and production stages. Theoretically, the efficiency of a bulk silicon solar cell is limited by the fixed band gap energy of this material<sup>1</sup>. In order to overcome this limitation, alternative structures such as tandem solar cells have been proposed<sup>2,3</sup>. In this tandem configuration, the bulk silicon is complemented with one or more solar cells presenting different band gap energies.

A suitable approach is a superlattice (SL) layer that is composed of ordered silicon nanocrystals (Si-NCs) embedded in a dielectric medium<sup>4</sup>. The functionality in this type of nanostructure is related to the Si-NC band gap energy, higher than the one of bulk silicon. The size and spatial distribution of the

Si-NCs and the surrounding dielectric media greatly influence the performance of the final photovoltaic device. Moreover, we know that some of the most important properties of the system are sensitive to subtle changes in the electronic properties of the single Si-NC, such as quantum confinement (QC) of charge carriers, as first discovered in porous Si<sup>5</sup>. Due to the QC effect, this value is inversely proportional to particle size. It is because of this property that control of NC size and environment is crucial for the final application of these nanostructures. In practice, this represents a complex problem given that the diameter of the particles should be typically below ~ 5 nm for the QC effect to be significant.

Beyond these morphological concerns, the experimental techniques that are commonly used for the assessment of performance in these systems – photo- and electroluminescence, charge transport measurements, Raman scattering spectroscopy, to name a few – do not allow us to get a direct functional characterization of the individual components. However, different techniques available in transmission electron microscopy (TEM) allow accessing these properties at high spatial resolution. In particular, high resolution (HR-) and energy filtered (EF-) TEM are the most commonly employed techniques. As a combination of structural and chemical characterization, EFTEM has been intensively used in the

<sup>a</sup> MIND-IN2UB, Departament d'Electrònica, Universitat de Barcelona, Martí i Franqués 1, 08028 Barcelona, Spain; E-mail: [aeljarrat@el.ub.edu](mailto:aeljarrat@el.ub.edu)

<sup>b</sup> Laboratorio de Microscopías Avanzadas (LMA) - Instituto de Nanociencia de Aragón (INA) and Departamento de Física de la Materia Condensada, Universidad de Zaragoza, 50018 Zaragoza, Spain

<sup>c</sup> Fundación ARAID, 50018 Zaragoza, Spain

<sup>d</sup> TEM-MAT, Centres Científics i Tecnològics (CCiT), Universitat de Barcelona, Solís i Sabarís 1, Barcelona, Spain

evaluation of the Si-NCs size after deposition<sup>3,6,7</sup>.

This work aims to characterize Si-NCs embedded in different dielectric materials by means of energy loss spectroscopy (EELS) data obtained from aberration corrected scanning transmission electron microscopy (STEM), using a monochromated sub-eV energy resolution probe. We present here an original methodological approach for EELS data treatment to elucidate the ultimate electrical properties of the Si-NCs. The reasons to propose this strategy stem from the nature of the sample, as will be explained in the following paragraph. The direct result of this approach is the separation of the low-loss EELS contribution of the Si-NCs by multivariate analysis methods. Indirectly, we will be able to obtain properties that are measured or calculated from low-loss EELS. In this sense, plasmon and band gap energies are measured from the shape of certain spectral features; complex dielectric functions and electron effective masses are derived from the spectrum. Three of the most common components in silicon-based photovoltaic devices, silicon dioxide (SiO<sub>2</sub>), silicon nitride (Si<sub>3</sub>N<sub>4</sub>) and silicon carbide (SiC) matrices, will be considered, demonstrating the robustness of the proposed methodology of data analysis.

The analyzed samples are multilayer stacks combining dielectric material and Si-enriched layers where Si-NCs precipitate during the post-deposition annealing treatment<sup>3,6,8</sup>. In this configuration, the Si-NCs are completely surrounded by the dielectric material, and it is unlikely to prepare an electro-transparent TEM specimen that will give a direct and pure Si-NC low-loss EELS measurement in a STEM experiment. In other words, surrounding material will be present over and/or under the NC in the TEM lamella, so that the incident e<sup>-</sup> will go through it and it will contribute to the EEL spectra in the NC region. The reason for this limitation is the size of the NCs, below 10 nm in diameter, and the geometry of the embedded particle and matrix system. Moreover, in our TEM experiments it was not possible to get a direct measurement of the pure contribution of the Si-NC to the spectra. As in the related literature<sup>9,10</sup>, all measured spectra present a mixture of nanoparticle and matrix contributions, at least. Nevertheless, in this work we show that indirect low-loss EELS calculations revealing the electronic and structural properties of the Si-NCs are feasible by the appropriate use of computational methods. In our case, factorization of the EELS spectrum image (SI) using multivariate analysis (MVA) algorithms, in combination with phase identification and segmentation techniques, enables to separate the contribution of the Si-NC to the EELS spectra. The selected algorithms, non-negative matrix factorization (NMF)<sup>11</sup>, and Bayesian linear unmixing (BLU)<sup>12</sup>, have been proven useful for the analysis of other signals present in the EELS spectrum such as surface plasmon resonances<sup>13</sup>, or core-loss edges<sup>14</sup>.

The following sections give a detailed description of the

studied systems and the experiments performed, as well as a precise account of the computational methods applied to EELS data to disentangle the electronic properties of Si-NCs at the nanoscale.

## 2 Experiment

The samples considered for the present study, designed as active layers for tandem solar cells, consist of silicon-based multilayer stacks combining stoichiometric- and Si-rich-based dielectric layers. Three dielectric materials were used as a barrier: SiO<sub>2</sub>, SiC and Si<sub>3</sub>N<sub>4</sub>. The respective non-stoichiometric layers were: silicon rich oxynitride, carbide and nitride (SRON, SRC and SRN). The layers were deposited by plasma-enhanced chemical-vapor deposition (PECVD) with thicknesses below 5 nm. After the deposition process, the Si excess is precipitated, and phase separation is induced in order to achieve the Si-NC formation. For this purpose, different accumulative annealing treatments are used, with temperatures ranging from 1100°C to 1150°C depending on the compound and, in the SiC sample, a previous annealing step at 600°C. The final goal is the formation of a silicon quantum dot superlattice, on top of a bulk silicon solar cell (see Fig. 1 for a diagram of the structure). More information regarding the NC superlattice preparation may be found in Ref. 8 for the SiO<sub>2</sub> sample, in Ref. 3 for the SiC sample and in Ref. 6 for the Si<sub>3</sub>N<sub>4</sub> sample.

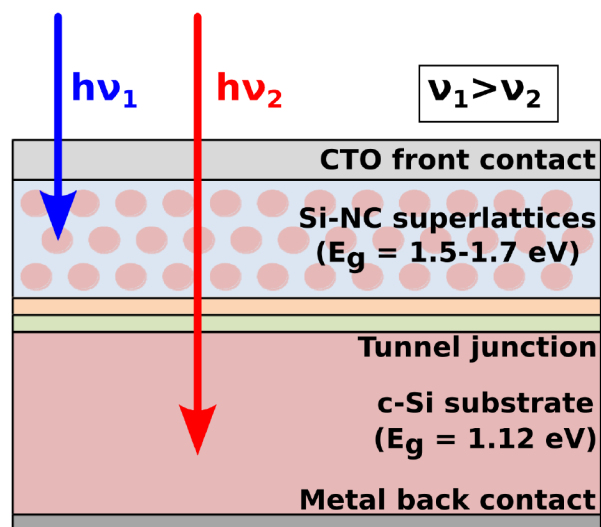


**Fig. 1** Tandem solar cell schematic diagram, showing the arrangement of the Si-NC superlattices on top of the c-Si solar cell. Arrows represent the incoming solar radiation, the high-energy photons (blue arrow) being absorbed by the higher band gap energy material, whereas the low-energy ones (red arrow) are absorbed within the c-Si bottom cell. CTO stands for conductive transparent oxide.

Electro-transparent samples for STEM observation in cross-section geometry were prepared by conventional mechanical polishing and low angle Ar<sup>+</sup> ion milling. In all cases, previous observations were performed in a JEOL J2010 F (S)TEM with a Schottky field emission gun operated at 200 keV. These measurements evaluated the quality of the fabricated multilayers, routinely measuring abruptness and homogeneity of the layers<sup>6,8,15</sup>. EFTEM experiments confirmed the formation of Si-NCs within alternative layers in the stack, and could give an average crystal size. As expected, crystal sizes were found to be related to the silicon-rich layer thickness, in our cases around or below 5 nm. From these first observations, it was clear that conventional electron microscopy would not suffice for the characterization of the Si-NCs and their environment.

Furthermore, some preliminary experiments indicated that higher voltages in STEM mode (*i.e.* 300 keV) and/or larger acquisition times could damage the Si-NCs and their environment, modifying or even destroying the studied structures in the process. Given the beam sensitivity of the Si-NCs, low accelerating voltages were used in the experiment. Moreover, as the experiment is usually designed to minimize radiation dosage by maximizing acquisition speed and reducing beam current density, the acquired spectral data may be affected by low signal to noise ratio (SNR). Nevertheless, since the plasmon signal is the strongest one in the EELS spectrum but for the zero loss peak (ZLP), the acquisition of low-loss EELS at low accelerating voltages and short acquisition times is feasible, in terms of SNR, when probing beam-sensitive materials. A probe-corrected FEI Titan 60-300 (S)TEM operated at 80 kV and equipped with a high-brightness field emission gun (X-FEG), a Wien filter monochromator and a Gatan Tridiem 866 ERS spectrometer was used to obtain the EELS data at high spatial resolution.

Three sets of low-loss EELS-SI and simultaneously acquired high-angle annular dark field (HAADF) images were obtained, from SiO<sub>2</sub>, SiC and Si<sub>3</sub>N<sub>4</sub> samples, respectively. A collection angle of ~ 2.5 mrad, a convergence angle of ~ 26 mrad, and an acquisition time of 0.03 s per spectrum were employed in the acquisition of the EELS data. Pixel sizes between 0.2-0.6 nm were selected for the EELS-SIs. The microscope conditions were thus adjusted to acquire HAADF-EELS datasets containing a few Si-NCs and a portion of the barrier layer. Exceptionally, for the silicon carbide sample, bigger datasets were acquired containing more than one period to portrait wider scale structural phenomena. Large areas of the specimens in relation to pixel size were covered in this way with no apparent beam damage. According to the full width at half maximum (FWHM) measured from the ZLP of the EELS-SI, energy resolution was kept below 0.2 eV in all experiments.

### 3 Analytical methodology

The large amount of raw data obtained for each system motivated the development of a simple, yet fast and powerful, computational treatment based on the prior identification of phase compositions through model based fitting and segmentation of the datasets by mathematical morphology techniques. In this way we analyzed a collection of EELS-SI with hundreds of pixels and 2048 spectral channels each.

A general treatment was applied to all datasets to retrieve information from the spatially localized spectra. The first part of the applied treatment is based on experience gathered through our recent works on low-loss EELS of semiconducting devices<sup>16,17</sup>, in which the characterization of the plasmon peak revealed structural and compositional information from the examined materials. Following a standard low-loss analysis scheme, all spectra had their energy axis calibrated using the ZLP and a measure of their relative thickness,  $t/\lambda$ , was obtained, from which the absolute thickness of the material can be estimated. This is important because plural scattering contribution to the spectra from thicker specimens can pose a problem to further analyses of the data. Additionally, a Fourier-log algorithm was used to produce single scattering distribution (SSD) spectra that can be compared to the original spectra to assess the impact of plural scattering.

#### 3.1 Identification and segmentation of data regions

The plasmon peak in bulk c-Si has an energy of ~ 16.7 eV, while the dielectric materials studied in this work have higher energy plasmons, ~ 22.5 eV for SiO<sub>2</sub>, ~ 23.7 eV for Si<sub>3</sub>N<sub>4</sub> and ~ 21.5 eV for SiC. This difference is large enough to distinguish each material by their characteristic plasmonic signature in the EELS spectra. An example of this, illustrated with EELS spectra from the SiO<sub>2</sub> sample, can be examined in Fig. 2(a) and (b). These spectra contain all the features that we examine in this work: the ZLP around 0 energy loss, the onset of valence transitions at low energies, and the plasmon peaks as the most intense feature in the low-loss region. Plasmon peaks were fitted, using a simple Lorentz model, with 2 fitting regions. These regions were selected according to the position of the low-loss maxima. As the Si-NC plasmon becomes apparent over the “pure dielectric” signal, the fit energy window is modified to adjust only the area around the Si-NCs plasmon. For each spectrum the fit window is centered on its intensity maximum, which is also a fitting parameter.

From the analysis of a given EELS-SI with this method, a plasmon energy,  $E_P$ , map is produced which we then analyze through a histogram thresholding approach. Our aim here is to identify regions of the dataset where spectra and their neighbors show “dominant Si-NC” or “pure dielectric” plasmonic features according to a defined threshold depend-

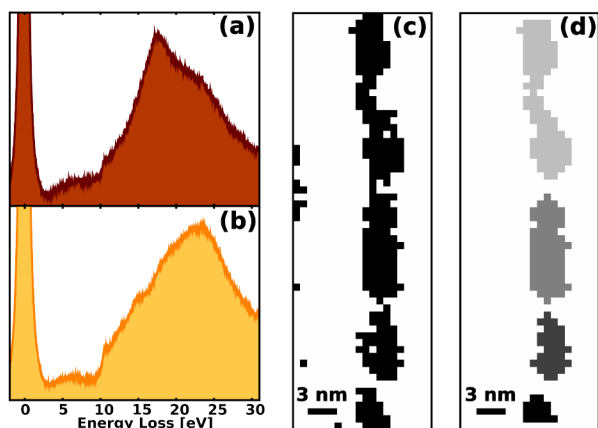


**Fig. 2** Panels (a) and (b) contain typical EELS spectra from the  $\text{SiO}_2$  sample, acquired at the Si-rich and barrier regions, respectively. Panel (c) shows a binary mask resulting from the thresholding of an EELS-SI from  $\text{SiO}_2$ . In this case, the pixels portrayed in black color have been found to contain spectra with  $E_p < 19$  eV. Panel (d) shows the map of individual elements labeled as “dominant Si-NC” regions generated from the previous mask after selecting only connected regions.

ing on the material. For this plasmon fingerprinting we impose the condition that a certain pixel of the  $E_p$  map (associated to a spectrum in the EELS-SI) is labeled as belonging to one of these two classes: the dominant Si-NCs (in fact a mixture of Si-NCs and the surrounding matrix) or the dielectric phase. However, the allocation of each pixel to a specific class (technically, Boolean masks, at this stage) generated by this approach alone may not be useful for various reasons. First, thresholding alone applied to an image may generate a mask including disconnected small spatial features, see Fig. 2(c), like separate regions of only a single or few pixels without physical meaning. Also, spatial features may appear to be connected, and identified as one alone although only joined by few pixels. Finally, it is desirable to identify big enough, yet separate, spatial features in the EELS-SI no matter what shape they may have. For this purpose, we developed an application in the framework of the Hyperspy toolbox\* that takes advantages of some computer vision tools included in the n-dimensional image analysis library of scientific Python (ndimage in SciPy). Operating over the binary identification maps, mathematical morphology operations act like a fast and powerful filter on the mask, allowing us to select the degree of connectivity required from the regions to be labeled. Namely, the  $E_p$  map is filtered using binary opening and closing operations, with a structural element that selects only connected regions. Once a filtered mask has been produced, see Fig. 2(d), the labels are assigned in a simple and straightforward step.

The result is the possibility to locate a spatial region of the original EELS-SI which spectra fulfill a certain requirement, then access it regardless of its shape, and operate with it as a separate sub-dataset with the same number of dimensions as the original dataset. Additionally, the size of the identified region is automatically measured as the number of pixels that fulfill the imposed condition.

After this procedure, a collection of sub-datasets allocated to the class of “dominant Si-NCs” or “pure dielectric” regions was generated. All the results presented in this work were achieved taking those regions as a starting point. For example, by averaging the spectra within them, noise-free spectra can be obtained that reveal the characteristic EELS features from the region. As will be shown in the following sections, using this strategy one can obtain material information or, depending on the case and region, get close estimates of the Si-NC or dielectric EELS data.

### 3.2 MVA factorization

Our analysis continued by focusing on the factorization of the low-loss EELS spectra by MVA within the detached subsets of data of the class “dominant Si-NCs” features. MVA factorization is performed by using computational tools that analyze a given matrix of spectral data and decompose it into a number of components. These components constitute additive contributions to a model of the EELS data, and are expressed as the product of corresponding factors and abundance maps. Factors have the same number of channels as the input EELS spectra and an associated abundance map indicating its spatial distribution, with the same number of pixels as the original EELS-SI. A legitimate guess is that one might be able to retrieve the contribution associated with the Si-NCs by performing a factorization of the whole EELS-SI by using MVA algorithms. It turns out that for most cases this is a difficult task because low-loss EELS is not always optimized as a direct input for MVA. The major reason for this is the fact that, in many cases, the presence of different phases in the examined materials translates into an energy shift of the plasmon peaks, associated with the transition between phases. This peak shift, which is usually an interesting subject of study, increases the number of dimensions for the factorization. As a result, multiple factors appear associated to a single shifting feature, hindering the interpretation of the results. With these limitations in mind, MVA factorization was performed on the aforementioned sub-datasets, which are characterized by the mixture of two competing contributions, the Si-NC plasmon peak over a dielectric-type background peak.

MVA factorization has been traditionally performed in the EELS community using decomposition by principal component analysis (PCA), followed by blind source separation (BSS) by independent component analysis (ICA)<sup>18–22</sup>. The

\*hyperspy.org

application of such an approach to low-loss EELS has an additional difficulty because the mutually independent sources assumption in ICA may not be necessarily fulfilled in the hyperspectral data. In this work we have used two different methods, the non-negative matrix factorization (NMF, included in Hyperspy)<sup>13</sup>, and the Bayesian linear unmixing (BLU, presented by the authors as a Matlab code)<sup>12,23</sup>. These two algorithms have in common the so-called positivity assumption, *i.e.* sources are supposed to be positive. This constraint fits well to the nature of EELS spectra, as no negative contribution is expected. Conversely, the BLU algorithm applies an extra additivity constraint to the sources, meaning that the sum of all contributions should be equal from pixel to pixel. Additionally, as this algorithm is initialized by a set of factors determined from a geometrical algorithm (N-FINDR in this work), the resulting set of factors is expected to be related to the ability to find pixels which contain the most pure spectral contributions as possible (least mixed pixels).

We added spike removal and Poisson normalization steps to the data prior to the application of any of these MVA algorithms [Keenan04]. In the first step, spikes are detected by thresholding the first derivative of the spectral data and removed by spline interpolation. In the second one, the Poissonian nature of the statistical distribution in EELS is taken into account, and data are normalized to approach a Gaussian distribution. With this normalization we expect to improve the suitability of the input data for the BLU algorithm, as a Gaussian statistical distribution is one of the hypothetical requirements for BLU. Both methods are also included in Hyperspy, and a Matlab application was developed in order to use the Poisson-normalized datacubes in conjunction with the BLU program.

### 3.3 Optoelectronic properties from EELS

Apart from the chemical information contained in the plasmon peak, low-loss EELS from a semiconductor specimen contains information from interband transitions, as well as the band gap of dielectric and semiconductor materials, among others. The methodology exposed so far allows us to obtain information from these in single EEL spectra and average spectra from the identified regions (direct measurements), and MVA factors (indirect measurements). Additionally, Kramers-Kronig analysis (KKA) was carried out on the spectra to demonstrate the extraction of the complex dielectric function (CDF). A link exists between the EELS and the CDF of a given bulk material based on the semi-classical formula for the single scattering distribution (SSD)<sup>24,25</sup>,

$$\text{SSD}(E) = \frac{I_0 t}{\pi a_0 m_0 v^2} \cdot \log[1 + \beta/\theta_E] \cdot \mathfrak{I}[-1/\varepsilon(E)] \quad (1)$$

Where  $I_0$  is the elastic scattering (ZLP) intensity,  $t$  is the

sample thickness,  $a_0$  is the Bohr radius,  $m_0$  is the electron rest mass,  $v$  is the electron velocity,  $\beta$  is the collection angle,  $\theta_E$  is the characteristic angle for inelastic scattering at a given energy loss  $E$ , and  $\varepsilon$  is the energy dependent CDF. Thus the pre-logarithmic factor, which will be called  $K$ , depends only on the ZLP intensity and the electron kinetic energy  $T$ . The logarithmic factor will be called the angular correction,  $\Theta(\beta, E)$ .

The first step in KKA is to normalize the SSD, which we obtain from the EELS spectrum of a thin sample to set  $\mathfrak{I}[-1/\varepsilon(E)]$ . For the normalization step of KKA we have used two main approaches depending on the availability of refractive index values. If this value is available, the sum-rule of the Kramers-Kronig relations allows us to calculate the constant part of the above formula,  $K$ ,

$$K = \left(1 - \frac{1}{n^2}\right)^{-1} \frac{2}{\pi} \int_0^\infty \frac{\text{SSD}}{\Theta(\beta, E)} \frac{dE}{E} \quad (2)$$

Also, this approach allows measuring the thickness of the sampled region from the expression of  $K$  in eq. 1. The refractive indices of all the bulk materials involved in this work are well known, so this approach may be used for the spectra from the dielectric barriers or the crystalline silicon substrate. However, the values to be used for the Si-NCs MVA factors are not clearly known, since  $n$  depends on particle size<sup>26</sup>. For this reason, we have developed an alternative approach for the normalization step that rests on the previous estimation of the absolute thickness of the sampled region<sup>27</sup>. In this thickness normalization step, we use the value of  $t$  calculated in an adjacent region, of known  $n$ ,

$$K = \frac{I_0 t}{\pi a_0 m_0 v^2} = \frac{I_0 t}{T \cdot 332.5} \left[ \frac{\text{nm}}{\text{keV}} \right] \quad (3)$$

Also, for each KKA a measure of the intensity (sum of channel values) of the ZLP is necessary. In the case of the MVA factors, this value is not directly available because the ZLP has to be cropped off or subtracted before MVA factorization. We measured and stored the  $t/\lambda$  values using the total and ZLP intensities,  $I_T$  and  $I_0$ , respectively, for each pixel. Using this value we can relate the integral of a given EELS signal,  $I_S$ , with the value of the ZLP intensity to which it would theoretically correspond using the following formula,

$$t/\lambda = \log(I_T/I_0) = \log(1 + I_S/I_0) \quad (4)$$

Hence, ZLP intensity values that are needed for the normalization step in the KKA of MVA factors can be estimated from the  $t/\lambda$  mean value in a region where the factor is the dominant spectral feature (highest abundance). The KKA algorithm used, with the two normalization options, is implemented for Hyperspy, and is available to the public through the development version of this toolbox. Also using this toolbox, every spectrum was prepared for KKA in a similar way;

first by subtraction of the modeled ZLP tail, then by an extension of the plasmon tail by interpolation of a power-law, with forced-negative exponent, up to the next power of two (4096 channels). Any spurious intensity levels remaining before or inside the ZLP subtraction window (typically set to [0.5,1] eV) was smoothed out using a Hanning taper.

The response of the material to incident electromagnetic radiation is represented by its CDF, which may be compared to other CDFs usually derived from optical measurements. From this result we have also derived electron effective masses for conduction electrons, using an analysis proposed in Ref. 28. This analysis is based on the relation between  $E_p$ , the electron concentration at this energy,  $n_{eff}$ , and the high frequency dielectric constant,  $\epsilon_\infty$ <sup>29,30</sup>,

$$m^* = \frac{n_{eff}\hbar^2}{E_p^2\epsilon_0\epsilon_\infty} \quad (5)$$

All these quantities can be measured or derived from the spectral data or the CDF in a straightforward way. For instance, the plasmon energy may be measured from the spectral data using a Drude model based fit. Meanwhile,  $\epsilon_\infty$  and  $n_{eff}$  are derived from the CDF of the material, also following Ref. 28. The electron effective mass derived from this formula is related to the electron mobility and determined by the shape of the conduction band near its bottom. Finally, a measurement of the atomic (molecular) density of electrons involved in the valence plasmon excitation is available if one provides the atomic (molecular) density of the studied material. This value was also obtained as a check of coherence for our calculations.

## 4 Results and discussion

Figure 3 shows some examples of EELS spectra for the three set of samples according to the different dielectric matrix ( $\text{SiO}_2$ ,  $\text{SiC}$  and  $\text{Si}_3\text{N}_4$  as labeled in the figure). For each matrix, a pair of spectra representative of the classes “Si-NCs” or “pure dielectric” (labeled as barrier) are drawn. In these plots, the raw spectra are presented as color-filled areas, and the black lines define the averaged spectra of a specific sub-data set of each class, identified following the segmentation procedure explained above. In the figure, the improvement of the SNR from raw to average spectra is evidenced. But interestingly enough, it is also noticed that the spectra from the class “dominant Si-NC regions” present significant differences depending on the matrix, revealing the impact of the different dielectric backgrounds.

Although this will increase the difficulty in analyzing and interpreting results from the spectra, EELS may be the less problematic STEM technique for extracting information arising solely from the Si-NCs. This was already pointed out in

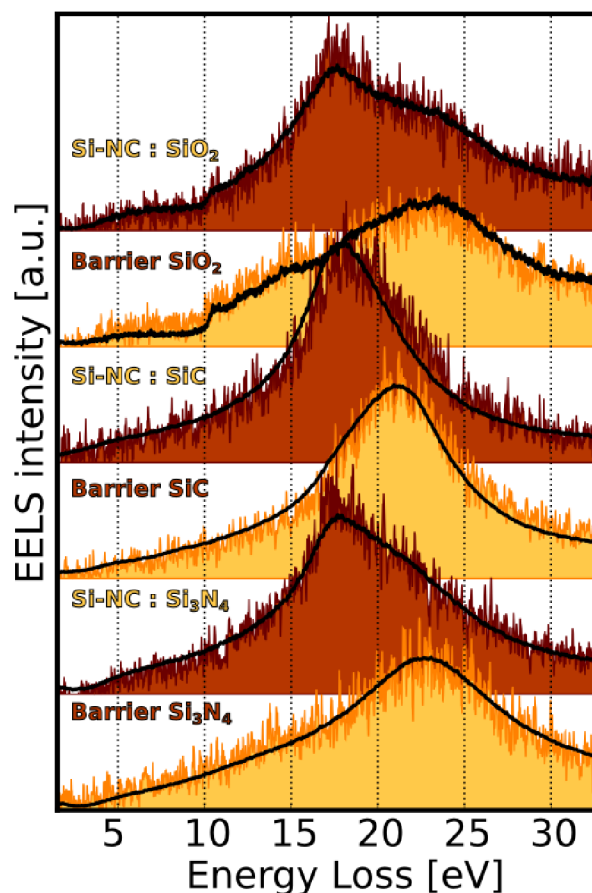


**Fig. 3** Raw (color-filled areas) and average (black lines) EELS spectra from the three examined samples. The spectra are averaged or extracted from regions identified as belonging to the class of “dominant Si-NCs” or to the class of “dielectric” using threshold values of the  $E_p$  plasmon distribution.

Ref. 9, where EELS was shown to be the appropriate technique for a complete and accurate structural characterization of the particles. Other methods were not a reliable source of structural and chemical information regarding the Si-NCs (BFTEM, HAADF, or  $t/\lambda$  imaging). Figures 4(a)-(c) present some examples of this, and will be thoroughly discussed in the following section.

### 4.1 Silicon oxide barriers

Figure 4 presents some results from one of the HAADF-EELS datasets corresponding to the  $\text{SiO}_2$  system. Fig. 4(a) shows the HAADF-STEM intensity image obtained in a region that contains both silicon enriched  $\text{SiO}_2$  layer and the  $\text{SiO}_2$  barrier, and Figs. 4(b) and (c) show the  $t/\lambda$  ratio and the  $E_p$  maps, respectively, as calculated from the corresponding EELS-SI. The faint contrast through the center of both HAADF and  $t/\lambda$

maps indicates the presence of the Si-rich layer. Also, the  $t/\lambda$  around 0.25 tells us that this is a very thin sample and that the impact of plural scattering to EELS should be low. An alternative to the  $E_p$  map is to represent the values of the  $E_p$  as a histogram of frequencies as shown in Fig. 4(d). The latter is useful to understand the color code in the map and to assess the  $E_p$  distribution. The two significant classes are easily distinguished in the histogram where  $E_p$  thresholds of 19 eV and 22.3 eV, indicated by lines in Fig. 4(d) and by region contours in Fig. 4(c), were selected to define the class of “dominant Si-NC” or “pure dielectric” features. Note also that the energy resolution of the experiment, indicated by the ZLP, is below 0.2 eV, the size of one bin in the histogram.

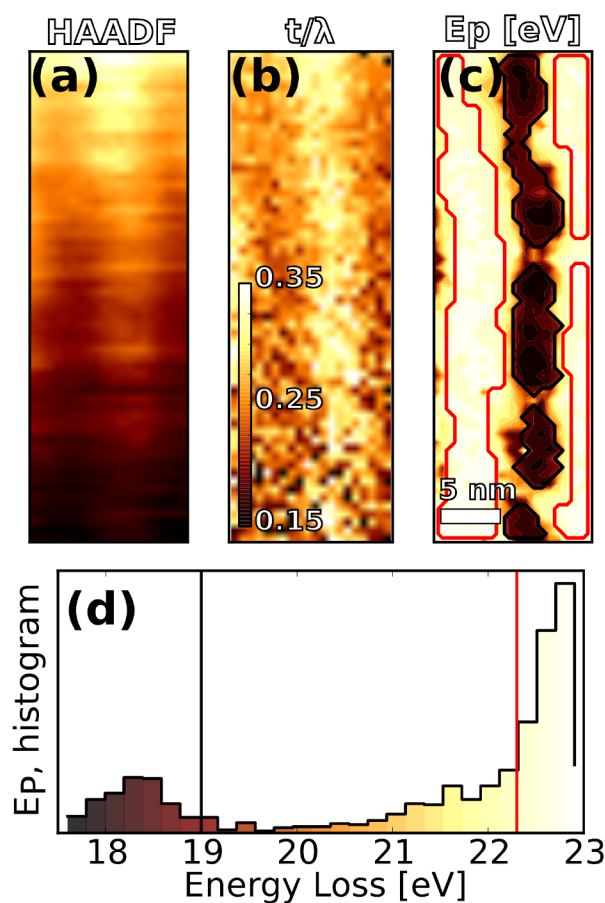


**Fig. 4** Panel (a) displays the HAADF intensity while (b) and (c) show the  $t/\lambda$  and  $E_p$ , respectively, of the simultaneously acquired EELS-SI from a  $\text{SiO}_2$  sample. Panel (d) shows the histogram corresponding to the  $E_p$  map in (c). In both last panels black and red lines indicate the threshold of the “dominant Si-NC” and “pure dielectric” regions. The generating process of these same “dominant Si-NC” regions was illustrated in Fig. 2.

The barriers and the Si-rich region seem to be well defined, with little variation of  $E_p$  through consistent areas. While  $E_p$

for these areas is below 23 eV, the corresponding plasmon maximum is  $\sim 23.7$  eV, due to the asymmetric shape of this peak. It is now clear that the examined area contains a full dielectric barrier, which spans along the left side of the image, a total of 4 Si-NC regions, featured at the center, and part of a second barrier, along the right side. The picture also shows that the extent of the dielectric layer and Si-rich layers has remained unchanged, both layers having  $\sim 5$  nm width. Similarly, the Si-NCs appear to be confined inside the Si-rich layer. Other areas of this  $\text{SiO}_2$  multilayer were scanned in the same fashion, showing similar results along the different periods.

Once the regions are defined, average spectra may be obtained from the pixels within. Two of these spectra, from the “dominant Si-NC” region in the center of the image and the “pure dielectric” barrier at the left side, are shown as black lines in the first two panels of Fig. 3. The raw spectra that are shown below the lines as color-filled areas were hand picked from one single pixel within these two region. Some features evidence the presence of a contribution from a dielectric-like inelastic scattering to the EELS in the Si-NC region. The major one is the presence of a shoulder at  $\sim 24$  eV that can be related to the  $\text{SiO}_2$  plasmon, present at this energy. Also, a strong peak onset at  $\sim 9.5$  eV and spanning several more eVs is detected, related with the band gap of  $\text{SiO}_2$ . This is in accordance with our picture of crystalline silicon particles embedded in a dielectric medium giving overlapped contribution to EELS, but not a direct confirmation.

However, MVA factorization by the NMF method proved to be useful as an indirect method for this confirmation. Let us use the specific region highlighted at the top of Fig. 4(c) to present the results. Fig. 5(a) shows the three main factors extracted from NMF. The contributions to the EELS from both dielectric and Si-NC phases are identified with the first two components. Using a RGB code we assign green color to the C1 component related to the Si-NCs, the red one to the component C2 associated with the dielectric contribution, and the blue color to C3, that reveals a sudden change in sensibility in the detector at a specific energy.

The number of factors used for NMF was chosen first by examination of the explained variance plot after PCA and second by comparison of the decomposition reconstructed signal with the spectra (residuals method). The plot in Fig. 5(b) illustrates this method, the two NMF reconstructed spectra (lines) and two raw spectra from the region show good accord.

The three left panels in Fig. 5 show the abundance maps corresponding to these three factors. Note also that these plots are rotated  $90^\circ$  clockwise with respect to the map in Fig. 4(c), and that a rotated  $E_p$  map included at the lower panel at the left hand side can be used as a reference. The spatial distribution of these components evidences two Si-NCs (in accordance to  $E_p$  map) with a variable dielectric background. The last component (blue) presents noise and the intensity step at the mid-

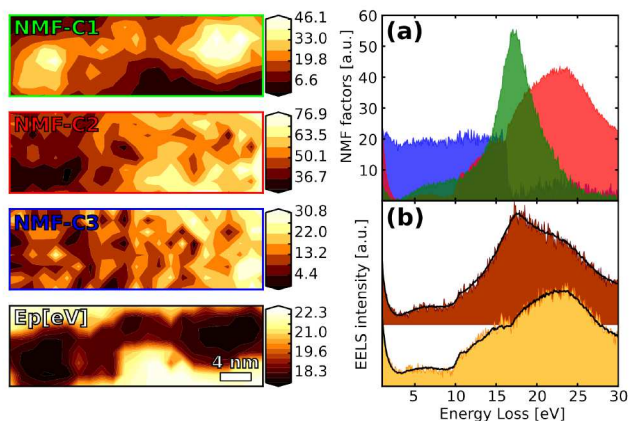


**Fig. 5** MVA analysis by NMF of Si-NCs in the oxide sample. In panel (a); main factors related to the Si-NCs (green), the dielectric barrier (red) and a detector concern (blue). The three upper left panels show the corresponding abundance of these factors using the same RGB color coding. Meanwhile, a reconstruction of the EELS from the decomposition model vs the raw EELS is shown at panel (b). Finally, a panel with the plasmon energy map for the same area is located at the lower left panel.

dle of the detector (channel number 1024) with a rather random spatial distribution and smaller abundance than the other two. Thus, this last component has a smaller relative weight than the first two.

In summary, the factorization reveals that the EELS contributions corresponding to the Si-NC and the SiO<sub>2</sub> matrix have plasmon maxima of  $\sim 17.3$  eV and  $\sim 22.7$  eV. The 1-eV energy shift between the SiO<sub>2</sub> in the barrier ( $\sim 23.7$  eV, plasmon maximum) and around the particle surroundings indicates the probable formation of a nitrogen oxide in the matrix, because of the growth process employing silicon rich oxynitride (SRON)<sup>8</sup>. The absence of further plasmon shifting within the barrier indicates a low and homogeneous diffusion of nitrogen from the SRON layers through the dielectric.

## 4.2 Silicon carbide barriers

For the SiC sample we succeeded in acquiring and analyzing large EELS-SI, with sizes up to more than  $120 \times 120$  pixels. The resulting  $t/\lambda$  and  $E_p$  maps are shown in Fig. 6. The area covered in this image spans over 3 periods of the multilayer (more than  $40 \times 40$  nm<sup>2</sup>), with a pixel-to-pixel resolution smaller than 0.4 nm. Smaller EELS-SI were also acquired and analyzed, as for oxide and nitride samples, but the use of a wider region was justified for studying a larger scale structural phenomenon in the carbide sample using the chemical sensitivity of low-loss EELS. Again,  $t/\lambda$  is used to confirm that the TEM sample is particularly thin at the examined re-

gion, around 0.25 times the electron inelastic mean free path,  $\lambda$ . No contrast related with the difference in  $\lambda$  from Si-NC and dielectric region is found in this image, Fig. 6(a). Nevertheless, some faint fringes can be distinguished at the center of the image, coming from the elastic scattering contrast in the ZLP intensity (equivalent to bright-field imaging), which are indicative of the presence of a crystalline particle. The simultaneously acquired HAADF image (not shown) showed weak contrast in relation to the Z-contrast of the silicon particles in the carbide medium, not useful for the characterization of neither particles nor barriers.

Figure 6(b), shows the  $E_p$  map with lines at the thresholds of 18.5 eV (red line) and 20.3 eV (black line) with a procedure similar to the one used for the previous sample, to depict the “dominant Si-NC” and “pure dielectric” regions, respectively. These numbers reflect the fact that silicon and silicon carbide plasmons are much closer than in the case of silicon oxide, for which the thresholds were 19 eV and 22.3 eV, respectively. The EELS spectra in the mid panels of Fig. 3, taken from Si-NC and dielectric regions, also evidence this closeness. From the examination of the maps obtained from this sample, we can tell that the dielectric barriers and silicon rich layers underwent some kind of segregation process. This process is first evidenced by the inhomogeneity of the interfaces between layers. Although the dielectric and silicon rich multilayer structure is preserved, the gradient of  $E_p$  values through the map evidences an unintended inter-diffusion of the layers in the growth direction. Also, attending to the energy resolution of the system, below 0.2 eV, the plasmon energies detected in the sample are only spatially consistent (meaning  $E_p$  values close to one of the expected values for the two classes) in small areas. In fact, the dielectric barriers do not always show pure silicon carbide energy, indicating that the diffusion from the silicon-rich layer modifies the chemical composition of the barrier layer. Finally, the inhomogeneity of the Si-NCs size is greater than in the other samples, with some coalescence and out-of-plane growth observed.

MVA factorization of the EELS data was also tested in this dataset, and the separation of a component related to the Si-NCs plasmon was possible. However, it was difficult or impossible to obtain a consistent component associated with the silicon carbide background. We suspect that a continuous change in the position of the silicon carbide plasmon caused by the variability in composition and the faulty separation of phases in the sample might be responsible for this. Thus, no MVA results are shown in this case. Nevertheless, it seems that the EELS low-loss features from this sample are sharp and differentiated when averaging inside the “dominant Si-NC” and “pure dielectric” regions (see Fig. 3). This indicates that the EELS contribution measured in the “dominant Si-NC” region has a much smaller impact in the dielectric phase than in SiO<sub>2</sub> and Si<sub>3</sub>N<sub>4</sub> samples, owing probably to the bigger size of

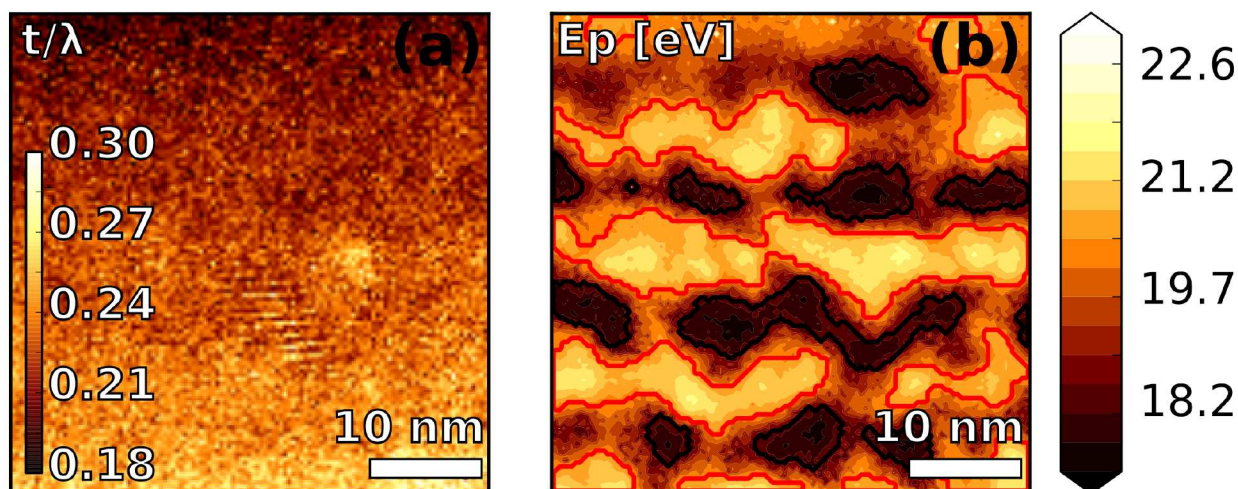


**Fig. 6** Panels (a) and (b) display the  $t/\lambda$  and  $E_p$  maps, respectively, calculated from the same EELS-SI of the carbide sample. Black and red lines are used, as in Fig. 4(c), as region boundaries.

the formed Si-NCs. Taking these considerations into account we generated some spatially averaged EELS spectra and examined them in order to identify both band gap and plasmon features. In these spectra a strong signal with an onset at  $\sim 2.5$  eV is evident, owing to the band gap energy of the SiC. No signal at lower energies could be consistently detected in this case. This indicates that the band gap signal of the Si-NCs, if present, is faint over the delocalized band gap signal of the surrounding SiC. For the plasmon peak, the contrast between the regions is clear in both energy and width. The barrier material from the center of the “pure dielectric” regions presents a broad plasmon peak at  $\sim 21.5$  eV. This peak transforms continuously to lower energies as we examine regions farther away, down to a sharp peak at  $\sim 17.5$  eV at the center of the “dominant Si-NCs” regions.

### 4.3 Silicon nitride barriers

As for the previous two samples, the silicon nitride multilayer was probed by HAADF-EELS acquisition and analyzed using a similar methodology. Fig. 7 presents three plasmon energy maps for this sample obtained in different regions of the multilayer stack. Black and red lines show the nature of the EELS plasmon in the enclosed regions, “dominant Si-NC” and “pure dielectric”, respectively. To obtain these, the same energy thresholds as in SiO<sub>2</sub>, 19 eV and 22.3 eV, have been used since the involved phases (Si-NC and Si<sub>3</sub>N<sub>4</sub>) show similar plasmon energies. Concerning the morphology, the configuration of barriers and Si-rich layers is preserved, as in the case of SiO<sub>2</sub>. However, for the Si<sub>3</sub>N<sub>4</sub> the contribution of the dielectric plasmon as a background to the EELS data in “dominant Si-NC” regions is not as evident as in the oxide case. This is because silicon nitride lacks the strong and characteristic low-energy

peaks of the silicon oxide EELS features.

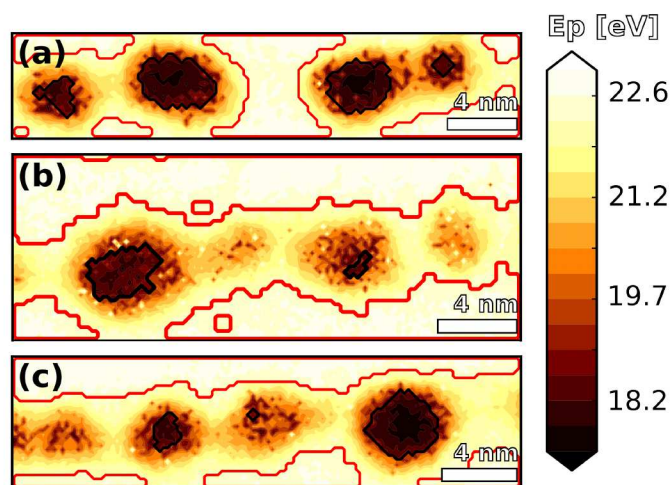


**Fig. 7** Panels (a)-(c) feature plasmon energy maps from different EELS-SI acquired in the nitride sample. Black and red lines are used, as in Fig. 4(c) and 6(b), as region boundaries.

Yet, MVA was able to separate the contributions of Si-NC and the dielectric background to the EELS data in the “dominant Si-NC” region. Fig. 8 shows an example of MVA analysis of the particle at the right hand side of Fig. 7(c). In this case we used a BLU algorithm with three components and a wider spatial crop in order to also include the dielectric regions on top and bottom of the particle. The resulting components show an analogous result to the NMF applied to SiO<sub>2</sub>. One of these components contained the Si-NC factor with abundance map localized around the particle, *i.e.* green factor in Fig. 8(a). The other two components contained the same dielectric back-

ground plasmon convolved with a small positive or negative intensity step from the detector. When they were added, this contribution canceled out leaving only the background peak, *i.e.* red factor in Fig. 8(a). We also observe good correspondence between the modeled spectra after decomposition and the raw spectra, depicted in Fig. 8(b). The contribution from the Si-NC particle in Fig. 8 is related to a plasmon energy of  $\sim 17.8$  eV. The barrier and matrix dielectric plasmon energies determined from averaging and factorization were measured at  $\sim 22.7$  eV. From this correspondence we expect the dielectric material from the barrier and particle surroundings to have a similar composition, just altered in the nearest vicinity of the Si-NC. In fact, some “pure dielectric” regions are found to exist in the silicon-rich layer, surrounding the Si-NCs, see Fig. 7(a), which supports this assumption.

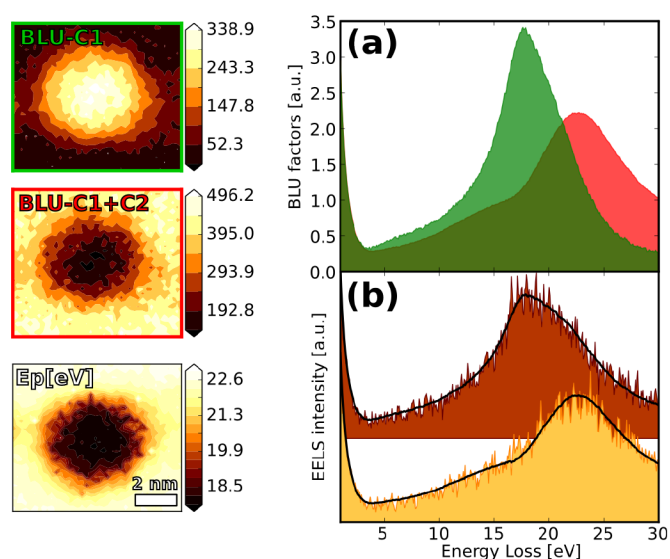


**Fig. 8** MVA analysis of Si-NCs in the nitride sample by BLU. Panel (a) shows estimated main factors related to Si-NCs (green) and a mixture of dielectric and instrument-related components (red). The two upper left panels show the abundance of the factors in panel (a), using the same red-green color coding. Meanwhile, a reconstruction of the EELS from the decomposition model vs the raw EELS is shown in panel (b). Finally, the plasmon energy map for the same area is located at the lower left panel.

From the  $E_P$  maps presented in Fig. 7 and the BLU abundance maps in Fig. 8, it seems that the particles formed in the silicon nitride matrix are rounder than the ones formed in silicon oxide (and, of course, carbide). We expect for the Si-NCs formed in  $\text{SiO}_2$  to occupy irregular volumes, as shown in the tomographic study of Ref. 9. Conversely, some of the Si-NCs in  $\text{Si}_3\text{N}_4$  are not completely formed while Si-NCs in  $\text{SiO}_2$  appear to have a very homogeneous distribution of sizes. It could be argued that their EELS signal is lower because much smaller Si-NCs are formed in  $\text{Si}_3\text{N}_4$  in comparison to other

systems. Nevertheless, no plasmon shift associated with the smaller size of these particles was found, indicating that these nanoparticles may not be fully crystalline.

Our plasmon energy measurements have to be interpreted in the context of QC theory, in which the plasmon peaks of Si-NCs show higher plasmon energy than that measured in c-Si ( $\sim 16.9$  eV). Ref. 10 proposes a phenomenological formula to relate plasmon energy with particle size in a case similar to ours. Following this formula, a plasmon energy of 17.8 eV is related to crystalline Si nanoparticles with diameters around 5.1 nm. In this sense, the obtained values are in excellent agreement with the previous results on plasmon energy shift from QC effects.

A final consideration about the measured Si-NC plasmon energies for all systems is that no consistent shift of this feature related with (apparent) particle size was found. Bearing in mind that QC effect implies an inverse relation between particle diameter and plasmon energy, this indicates that crystalline particle sizes and environments are similar throughout each sample. The different apparent size occupied by each “dominant Si-NC” region in the  $E_P$  map may be identified with the real size of a separate particle. However, our measures indicate that as the Si-NC plasmon energies for these regions are similar, they must contain Si-NCs of similar real size, according to QC. This contradicts in many cases the judgment that one could, a priori, extract from the examination of the apparent sizes of the particles in the raw plasmon energy images.

These considerations do not affect our belief that the separation between particle and surrounding material, in terms of EELS signal, has been proven feasible. One of the main reasons is the smaller delocalization distance for the quantum-confined Si-NC plasmon than for the band gap. Also, the relatively small difference between the dielectric functions of the Si-NCs and surrounding materials, which will be calculated in the following section, diminishes the effects of interface plasmons<sup>31</sup>. We should also mention that for any MVA technique, peak energy shifting and the existence of an intense background signal would affect negatively the final result<sup>32</sup>. In low-loss EELS we easily get both effects, the shifting of the plasmons linked to gradients in concentration or strain being a well-known feature in a wide range of samples. To complete the list, ZLP intensity is typically several orders of magnitude above any other feature in low-loss EELS data. This means that MVA techniques are unsuitable to solve problems in which a continuous plasmon shift is a dominant feature or in which the ZLP masks out the desired feature, like in low-lying band gap energies. In our case, the energy stability of the plasmons in selected areas and the correct alignment of the ZLP and energy windows before the MVA have been the key to enable the successful NMF and BLU analyses.

To summarize, we have presented three different cases where the analysis of EELS maps is an advantageous tech-

nique when compared to other TEM-based approaches, although convolution of the interesting features is an inherent difficulty. In previous works, a model-based fit containing two Drude plasmons approach proved also reliable<sup>33</sup>. Nevertheless, when applied on these systems it fails to give consistent measurements of neither  $E_p$  nor width for all the studied systems. Our present experience indicates that this double plasmon model will only be reliable when the fitted features are well separated in energy and exhibit significant differences in FWHM, *i.e.* low energy narrow peak vs high energy wide peak (as in the case of Si-NCs in a SiO<sub>2</sub> matrix). Conversely, when analyzing plasmonic features that are very close in energy and width, this method may not be reliable and may lead to uninterpretable or wrong results (as in Si-NCs in SiC and Si<sub>3</sub>N<sub>4</sub> matrices). Other works that have examined Si-NCs in a silicon nitride matrix using a model-based fit analysis of EELS data found much higher variability of the calculated plasmon energy data for the background<sup>10</sup>. Moreover, an additional disadvantage is that EELS data acquired from thin specimens will be naturally noisy as the inelastic scattering signal is diminished. In spite of all these difficulties, our phase identification and segmentation technique, complemented with factorization by NMF and BLU algorithms, has proved to be capable of extracting valuable information. The following and last section will be devoted to the more complex aspects of the low-loss analysis.

#### 4.4 Optoelectronic properties of the Si-NCs

KKA was used to calculate the CDF from the available spectra, namely, the “pure dielectric” region averaged spectra, the Si-NC and dielectric background spectra from MVA factors, and crystalline silicon (c-Si) single spectra acquired from the substrate (see Fig. 9).

On both silicon oxide and nitride cases, the first step was to perform KKA on the spectra identified as dielectric signals, using the corresponding refractive index for each material<sup>34</sup>,  $n_{\text{SiO}_2} = 1.5$  and,  $n_{\text{Si}_3\text{N}_4} = 2$ . For the MVA factors, the ZLP intensities were calculated from the signal integral and a mean of the calculated  $t/\lambda$  from a selected “pure dielectric” region of the EELS dataset. Both dielectric CDFs, from MVA factors and average spectra, showed excellent accordance with one another.

These CDFs are depicted in Fig. 9(a) and (b); note that while the correspondence for silicon nitride is almost perfect, the silicon oxide functions differ in their intensity and plasmon position. This is an expected result, as the EELS average spectrum from the barrier region (SiO<sub>2</sub>) differs in plasmon position and width from the EELS contribution from the dielectric surrounding the Si-NC (SRON). Sample thickness values were obtained thanks to the use of the  $t/\lambda$  value for the normalization. Both samples were confirmed to be particularly thin at

the examined regions, with  $t \sim 48$  nm and  $t \sim 18$  nm for the silicon oxide and nitride matrices, respectively. This value is used for the normalization step in the KKA of the MVA factors identified as Si-NC signals. Again, the  $t/\lambda$  mean values for the dominant Si-NC regions linked the signal integral with the ZLP intensity. It was found that this value is typically bigger than in the dielectric region, indicating a decrease in the electron mean free path,  $\lambda$ , associated with the presence of the Si-NC. The Si-NC CDFs were then calculated, see Fig. 9(c), showing good agreement between the results for both particles within the silicon oxide and nitride matrices. For the sake of completeness we also applied KKA to retrieve the CDF from a single spectrum acquired at the c-Si substrate in the silicon nitride system, see Fig. 9(c).

An inherent disadvantage of measuring optoelectronic properties using EELS is the difficulty to recover the information lying at very low energies (*e.g.* band gaps, typically below 5 eV), due to the rather intense tails of the ZLP. However, we have been able to measure band gap energies in our samples and to add this information to our derived CDF, thanks to the good energy resolution in our experiments (*i.e.* ZLP FWHM below 0.2 eV). For the silicon oxide barrier sample, the band gap feature of SiO<sub>2</sub> is observed at  $\sim 10$  eV, in good accordance with literature<sup>35</sup>. This value is also in good accordance with our idea of low and homogeneous nitrogen diffusion from the silicon rich layer (SRON) to the SiO<sub>2</sub> in the barrier.

The band gap in Si<sub>3</sub>N<sub>4</sub>, measured at  $\sim 4$  eV, is lower than the 5 eV value expected from the pure dielectric. Anyhow, this is already in accordance with the measured plasmon energy shift in the barriers from the expected 23.7 eV to the obtained 22.7 eV. We can postulate the formation of a SiN<sub>x</sub> ( $x < 1$ ) type matrix, and a general growth mechanism for the Si-NCs from nucleation until a critical size after which coalescence takes over, as in Refs. 10,36,37. The authors of those works attributed the decrease in plasmon energy to an increase of Si-Si bond concentration in the material. Our measurement of both plasmon and band gap energies exhibit a solidary redshift of  $\sim 1$  eV, indicating a consistent energy shift of the whole band structure near the Fermi energy or the addition of new levels<sup>38-40</sup>. Additionally, other works<sup>6</sup>, on similar samples measured by EFTEM, estimated that 15% of the volume of the dielectric barrier is distributed around the Si-rich layer and around the Si-NC. This measurement is in good accordance with our observations, *e.g.* “pure dielectric” region in between particles at Fig. 7(a).

The indirect band gap for c-Si is found at energies between 1.2-1.4 eV, and it is possible to measure this signal in the EELS spectra from bulk samples<sup>41</sup>. We confirmed the ability of our system to obtain this measurement using c-Si spectra acquired at the substrate of the samples. The CDF from c-Si substrate is shown in Fig. 9(c) (note the onset of the imaginary part). One may expect to detect a similar indirect band gap signal

also in the case of an embedded particle system. In the case of the Si-NCs, we should expect this signal to appear at higher energies, owing to quantum confinement<sup>26</sup>, but below 2-3 eV. However, no such feature was found in any of the Si-NC regions in the SiO<sub>2</sub> and Si<sub>3</sub>N<sub>4</sub> systems. It was also impossible to measure any consistent contribution to the spectral intensity levels below  $\sim 3$  eV for the Si-NC MVA factors or average spectra from the “dominant Si-NC” regions. We believe that the lack of the silicon indirect band gap signal in these embedded-particle systems should be attributed to the fact that particle dimensions are comparable to the electron delocalization distance, of  $\sim 10$  nm for the spectrum at low energy losses<sup>19,25</sup>.

Arguably, this does not exclude the possibility that a contribution from the indirect band gap is present in our low-loss EELS data. On one hand, this contribution would be among the less intense in the low-loss range, making it difficult to detect above the tail of the ZLP, the band gap signal from the surrounding material, and the noise level. On the other hand, we cannot neglect the possibility that electron energy losses apart from the ones related with the semi-classical interpretation of inelastic scattering may have an impact in the measured EELS spectra (see eq. 1). García de Abajo treats many of these cases<sup>24</sup>, among them the excitation of Čerenkov radiation and the case of a composite material in which the grain size affects the interface-to-volume loss ratio. Although we are not able to consistently measure such contributions and the use of a low energy beam (80 keV) theoretically reduces the possibility for Čerenkov radiation excitation, we cannot discard the possibility that a mixture of spurious losses could be affecting the measurement of the indirect band gap. Surface losses, which relative importance increases as sample thickness decreases, were subtracted in the usual way in the KKA algorithm<sup>25</sup>. The fact that surface loss contribution is relatively more important in the thinner Si<sub>3</sub>N<sub>4</sub> sample meant that KKA algorithm required more iterations (10 instead of 5 in the case of the Si-NC CDF) to reach proper convergence. Finally, the shape and energy of the features detected at  $\sim 3$ -3.5 eV allows us to relate this measurement to the Tauc optical absorption gap, the direct band gap feature of the Si-NC<sup>26,42,43</sup>.

Again, these results are in good correspondence with the QC model for Si-NCs of this size range. Although recent reports have stated that the electronic properties for small Si-NCs could exhibit smaller band gaps than the quantum-confined ones<sup>44</sup>, we believe these additional features will only be of importance in Si-NCs which size is around or below the 1 nm range. In this case it would be troublesome to characterize this effects, as the low-loss EELS from particles of such a small size will be affected very strongly by delocalized scattering from the surrounding material.

The electron effective mass,  $m^*$ , related to carrier mobility can be derived from the CDF<sup>28</sup>. For the Si-NC in silicon oxide

and nitride matrices,  $m^*$  values of  $0.129m_0$  and  $0.133m_0$  ( $m_0 = 9.11 \cdot 10^{-31}$  kg) were obtained, respectively. Meanwhile, for the c-Si substrate, a value of  $0.1m_0$  was obtained. By supposing an equal atomic density for c-Si and Si-NC of  $50.2 \text{ nm}^{-3}$ , an atomic density of electrons,  $n_{eff}$ , of  $\sim 3$  electrons was obtained, actually higher for the Si-NCs, up to 3.5, in Si<sub>3</sub>N<sub>4</sub>. In the case of crystalline silicon, as the k-space surfaces of constant energy are ellipsoids, this quantity consists of a combination of the transversal and longitudinal electron effective masses. The generally accepted value of  $m^*$  for c-Si is  $0.26m_0$ , with a valence electron density of 4 electrons per atom<sup>45</sup>. Note that the obtained  $m^*$  and  $n_{eff}$  values are below the expected. This appears to be a general trend for EELS measurements, as in the work of Ref. 28, where the  $m^*$  and  $n_{eff}$  calculated values for III-V nitride samples were smaller than the theoretically expected ones. However, the good correspondence with other techniques and the possibility to combine the chemical information also present in the spectra justify the use of EELS for the calculation of  $m^*$  values. Moreover, our calculation indicates an approximate correspondence of the values for c-Si and the Si-NCs, with an increase of the  $m^*$  and  $n_{eff}$  in the Si-NCs.

**Table 1** Summary of the bandgap and plasmon energies and the electron effective masses, obtained for the three different samples in regions of interest. Note that for SiO<sub>2</sub> and Si<sub>3</sub>N<sub>4</sub>, the values presented from barrier regions are obtained by averaging, while the ones from matrix and Si-NC regions are obtained by MVA. For SiC, only averaging is used, as explained in the text.

Region		$E_B/\text{eV}$	$E_P/\text{eV}$	$m^*/m_0$
SiO <sub>2</sub>	Barrier	9.5	23.7	—
	Matrix	9.5	22.7	0.188
	Si-NC	3.0	17.3	0.129
SiC	Barrier	2.5	21.5	—
	Si-NC	—	17.5	—
Si <sub>3</sub> N <sub>4</sub>	Barrier	4.0	22.7	—
	Matrix	4.0	22.7	0.160
	Si-NC	3.5	17.8	0.133
c-Si substrate		1.3	16.9	0.1

## 5 Conclusions

Our phase identification and segmentation technique proved that a selective averaging of spectra from regions allocated to a specific “dominant Si-NC” or “pure dielectric” class, can enhance the SNR in spectra, thus preserving the features of the EELS spectrum containing valuable information about the probed regions. We showed how MVA can be used to disentangle the individual spectral contributions to the characteristic EELS spectrum of the embedded particle system: the

Si-NC and background dielectric signals.

The plasmon energies measured in the SiO<sub>2</sub> barriers are consistent with literature and indicate mostly pure dielectric barriers that do not suffer from such effects as inhomogeneous silicon or nitrogen diffusion. Conversely, in the case of SiC and Si<sub>3</sub>N<sub>4</sub> barrier systems, the significant shifts of the plasmon energy indicate an overall inhomogeneity in composition that can be related to the diffusion of silicon from the Si-rich layer. Moreover, the inhomogeneous shape and distribution of Si-NCs in the SiC sample as compared with the other two indicates that diffusion severely affected the shape of the multilayer structure, with generalized coalescence of the Si-NCs and deformation of the barrier interfaces.

In the SiO<sub>2</sub> case, NMF allowed separating a spurious intensity step in the detector and recovering each contribution as a separate component. This was not possible in the Si<sub>3</sub>N<sub>4</sub> case, in which we showed that BLU allowed for the separation of the Si-NC contribution in one component whereas two other components contained the mixed contributions from dielectric plasmon and intensity step. The different results after applying NMF or BLU highlight the differences between both techniques, *i.e.* the geometrical initialization and additivity constrain of BLU. Both analyses were enabled by the previous use of spike removal and Poisson normalization steps.

A detailed report on the electronic analysis of the EELS data and the derived MVA factors was given. Different KKA normalization steps were employed, using the refractive index or the thickness, depending on the available data. The derived CDFs of the dielectric material in the barriers, the dielectric material surrounding the Si-NCs, and the Si-NCs themselves provided a valuable insight into the structural properties of the systems after the growth process. These CDF were compared to the CDF from a c-Si substrate area. Good accordance between the compared CDFs was found, and plasmon and band gap energies (including quantum confinement effect within the Si-NCs) were taken into account for an optoelectronic characterization of the materials. Finally, electron effective masses and approximate density of electrons for c-Si and the Si-NCs have been calculated and compared with the expected values.

## Acknowledgments

Electron microscopy characterization has been carried out using the TEM facilities of the “Scientific and Technological Centres” (Universitat de Barcelona) and the “Laboratorio de Microscopías Avanzadas” at “Instituto de Nanociencia de Aragón” (Universidad de Zaragoza). The authors acknowledge LMA-INA for offering access to their instruments and expertise. The research leading to these results has received funding from the European Community’s Seventh Framework Programme (FP7/2007-2013) under Grant Agreement No: 245977, under the project title NASCEnT. The present work

was supported by the Spanish national projects MAT2010 numbers 16116 and 16407, and CSD-2009-0013 and also by the Catalan government through projects CAM (P2009/ESP-1503), and SGR2014-672.

## References

- 1 F. Meillaud, A. Shah, C. Droz, E. Vallat-Sauvain and C. Miazza, *Solar Energy Materials and Solar Cells*, 2006, **90**, 2952 – 2959.
- 2 G. Conibeer, M. Green, E.-C. Cho, D. König, Y.-H. Cho, T. Fangsuwanarak, G. Scardera, E. Pink, Y. Huang, T. Puzzer, S. Huang, D. Song, C. Flynn, S. Park, X. Hao and D. Mansfield, *Thin Solid Films*, 2008, **516**, 6748 – 6756.
- 3 J. López-Vidrier, S. Hernández, J. Samà, M. Canino, M. Allegranza, M. Bellettato, R. Shukla, M. Schnabel, P. Löper, L. López-Conesa, S. Estradé, F. Peiró, S. Janz and B. Garrido, *Materials Science and Engineering: B*, 2013, **178**, 639 – 644.
- 4 M. Zacharias, J. Heitmann, R. Scholz, U. Kahler, M. Schmidt and J. Bläsing, *Applied Physics Letters*, 2002, **80**, 661–663.
- 5 L. T. Canham, *Applied Physics Letters*, 1990, **57**, 1046–1048.
- 6 A. Zelenina, S. A. Dyakov, D. Hiller, S. Gutsch, V. Trouillet, M. Bruns, S. Mirabella, P. Löper, L. López-Conesa, J. López-Vidrier, S. Estradé, F. Peiró, B. Garrido, J. Bläsing, A. Krost, D. M. Zhigunov and M. Zacharias, *Journal of Applied Physics*, 2013, **114**, 184311.
- 7 S. Hernández, J. López-Vidrier, L. López-Conesa, D. Hiller, S. Gutsch, J. Ibáñez, S. Estradé, F. Peiró, M. Zacharias and B. Garrido, *Journal of Applied Physics*, 2014, **115**, 203504.
- 8 J. López-Vidrier, Y. Berencén, S. Hernández, O. Blázquez, S. Gutsch, J. Laube, D. Hiller, P. Löper, M. Schnabel, S. Janz, M. Zacharias and B. Garrido, *Journal of Applied Physics*, 2013, **114**, 163701.
- 9 A. Yurtsever, M. Weyland and D. A. Muller, *Applied Physics Letters*, 2006, **89**, 151920.
- 10 P. D. Nguyen, D. M. Kepaptsoglou, Q. M. Ramasse and A. Olsen, *Phys. Rev. B*, 2012, **85**, 085315.
- 11 C.-J. Lin, *Neural Computation*, 2007, **19**, 2756–2779.
- 12 N. Dobigeon, S. Moussaoui, M. Coulon, J.-Y. Tourneret and A. Hero, *Signal Processing, IEEE Transactions on*, 2009, **57**, 4355–4368.
- 13 O. Nicoletti, F. de la Pena, R. K. Leary, D. J. Holland, C. Ducati and P. A. Midgley, *Nature*, 2013, **502**, 80–84.
- 14 L. Yedra, A. Eljarrat, J. M. Rebled, L. López-Conesa, N. Dix, F. Sánchez, S. Estradé and F. Peiró, *Nanoscale*, 2014, **6**, 6646–6650.
- 15 C. Summonte, M. Allegranza, M. Bellettato, F. Liscio, M. Canino, A. Desalvo, J. López-Vidrier, S. Hernández, L. López-Conesa, S. Estradé, F. Peiró, B. Garrido, P. Löper, M. Schnabel, S. Janz, R. Guerra and S. Ossicini, *Solar Energy Materials and Solar Cells*, 2014, **128**, 138 – 149.
- 16 A. Eljarrat, S. Estradé, v. Gačević, S. Fernández-Garrido, E. Calleja, C. Magén and F. Peiró, *Microscopy and Microanalysis*, 2012, **18**, 1143–1154.
- 17 A. Eljarrat, L. López-Conesa, C. Magén, v. Gačević, S. Fernández-Garrido, E. Calleja, S. Estradé and F. Peiró, *Microscopy and Microanalysis*, 2013, **19**, 698–705.
- 18 A. Hyvärinen and E. Oja, *Neural Networks*, 2000, **13**, 411 – 430.
- 19 M. Bosman, L. J. Tang, J. D. Ye, S. T. Tan, Y. Zhang and V. J. Keast, *Applied Physics Letters*, 2009, **95**, 101110.
- 20 F. de la Peña, M.-H. Berger, J.-F. Hochepeid, F. Dynys, O. Stephan and M. Walls, *Ultramicroscopy*, 2011, **111**, 169 – 176.
- 21 T. Yamazaki, Y. Kotaka and Y. Kataoka, *Ultramicroscopy*, 2011, **111**, 303 – 308.
- 22 J. Bioucas-Dias, A. Plaza, N. Dobigeon, M. Parente, Q. Du, P. Gader and J. Chanussot, *Selected Topics in Applied Earth Observations and Remote Sensing, IEEE Journal of*, 2012, **5**, 354–379.
- 23 N. Dobigeon and N. Brun, *Ultramicroscopy*, 2012, **120**, 25 – 34.

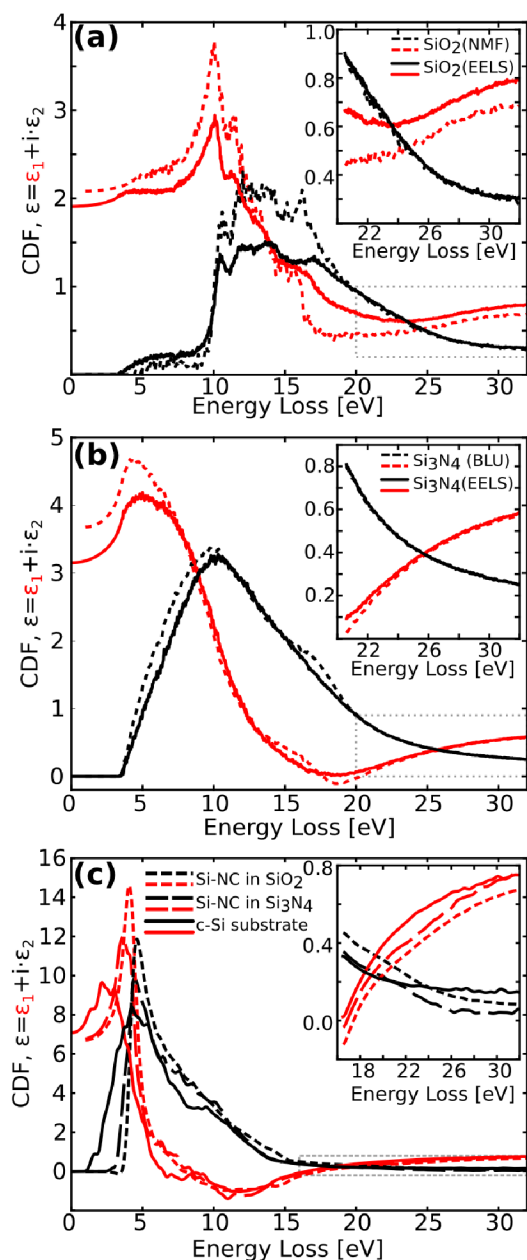


**Fig. 9** This figure shows CDF calculated from the KKA of experimental EELS spectra and MVA factors. In all of them, the real and imaginary parts of the CDF are indicated with red and black colors, respectively. Panels (a) and (b) contain the CDF calculated from silicon oxide and nitride; EELS spectra from the regions (solid lines) or, NMF and BLU factors (dashed lines), respectively. Panel (c) contains the Si-NCs CDF calculated from NMF and BLU, from the oxide and nitride samples, respectively, in dashed lines. Also in this panel is the CDF from the EELS spectrum of c-Si substrate, in solid lines. The insets show in detail the higher energy parts of the CDFs, marked using dashed line squares.

- 24 F. J. García de Abajo, *Rev. Mod. Phys.*, 2010, **82**, 209–275.
- 25 R. Egerton, *Electron Energy-Loss Spectroscopy in the Electron Microscope*, Springer US, 2011.
- 26 R. Guerra, F. Cigarini and S. Ossicini, *Journal of Applied Physics*, 2013, **113**, 143505.
- 27 D. T. L. Alexander, P. A. Crozier and J. R. Anderson, *Science*, 2008, **321**, 833–836.
- 28 M. H. Gass, A. J. Papworth, R. Beanland, T. J. Bullough and P. R. Chalker, *Phys. Rev. B*, 2006, **73**, 035312.
- 29 W. G. Spitzer and H. Y. Fan, *Phys. Rev.*, 1957, **106**, 882–890.
- 30 H. R. Chandrasekhar and A. K. Ramdas, *Phys. Rev. B*, 1980, **21**, 1511–1515.
- 31 V. J. Keast and M. Bosman, *Materials Science and Technology*, 2008, **24**, 651–659.
- 32 M. Bosman, M. Watanabe, D. Alexander and V. Keast, *Ultramicroscopy*, 2006, **106**, 1024 – 1032.
- 33 A. Eljarrat, L. López-Conesa, J. M. Rebled, Y. Berencén, J. M. Ramírez, B. Garrido, C. Magén, S. Estradé and F. Peiró, *Nanoscale*, 2013, **5**, 9963–9970.
- 34 E. Palik, *Handbook of optical properties of solids*, Academic, Orlando, 1985.
- 35 M. Couillard, A. Yurtsever and D. A. Muller, *Phys. Rev. B*, 2008, **77**, 085318.
- 36 F. Delachat, M. Carrada, G. Ferblantier, A. Slaoui, C. Bonafos, S. Schamm and H. Rinnert, *Physica E: Low-dimensional Systems and Nanostructures*, 2009, **41**, 994 – 997.
- 37 F. Delachat, M. Carrada, G. Ferblantier, J.-J. Grob and A. Slaoui, *Nanotechnology*, 2009, **20**, 415608.
- 38 P. E. Batson and J. R. Heath, *Phys. Rev. Lett.*, 1993, **71**, 911–914.
- 39 Y. W. Wang, J. S. Kim, G. H. Kim and K. S. Kim, *Applied Physics Letters*, 2006, **88**, 143106.
- 40 V. Gritsenko, H. Wong, J. Xu, R. M. Kwok, I. P. Petrenko, B. A. Zaitsev, Y. N. Morokov and Y. N. Novikov, *Journal of Applied Physics*, 1999, **86**, 3234–3240.
- 41 L. Gu, V. Srot, W. Sigle, C. Koch, P. van Aken, F. Scholz, S. B. Thapa, C. Kirchner, M. Jetter and M. Rühle, *Phys. Rev. B*, 2007, **75**, 195214.
- 42 J. Tauc, R. Grigorovici and A. Vancu, *physica status solidi (b)*, 1966, **15**, 627–637.
- 43 Z. Zhang, M. He and Q. Li, *Solid State Communications*, 2009, **149**, 1856 – 1859.
- 44 H. Vach, *Nano Letters*, 2011, **11**, 5477–5481.
- 45 P. Yu and M. Cardona, *Fundamentals of Semiconductors: Physics and Materials Properties (Graduate Texts in Physics)*, 2010.